



Crack Propagation in Hollow Cylindrical Specimen Undergoing Multiaxial Fatigue

Journal:	<i>Fatigue & Fracture of Engineering Materials & Structures</i>
Manuscript ID	FFEMS-7623
Manuscript Type:	Original Contribution
Date Submitted by the Author:	10-Jul-2018
Complete List of Authors:	Lepore, Marcello Antonio; university of salerno, Dept. of Industrial Engineering Yarullin, Rustam; Russian Academy of Sciences, Researches Center for Power Engineering Problems maligno, angelo; University of Derby Sepe, Raffaele; University of Naples Federico II, Dept. of Chemical, Materials and Production Engineering

SCHOLARONE™
Manuscripts

Crack Propagation in Hollow Cylindrical Specimen Undergoing Multiaxial Fatigue

M. Lepore^a, R. Yarullin^b, A. R. Maligno^c, R. Sepe^{d*}

^aDept. of Industrial Engineering, University of Salerno, Via G. Paolo II, 132 - 84084 Fisciano, Italy.

^bKazan Scientific Center of Russian Academy of Sciences, Lobachevsky Street, 2/31 - 420111 Kazan, Russia.

^cInstitute for Innovation in Sustainable Engineering, University of Derby, Derby, UK.

^dDept. of Chemical, Materials and Production Engineering, University of Naples Federico II, P.le V. Tecchio 80, 80125 Naples, Italy.

Abstract: Three-dimensional numerical analyses, using the Finite Element Method (FEM), have been adopted to simulate fatigue crack propagation in a hollow cylindrical specimen, under pure axial or combined axial-torsion loading conditions. Specimens, made of Al alloys B95AT and D16T, have been experimentally tested under in-phase constant amplitude axial and torsional loads. The Stress Intensity Factors (SIFs) have been calculated, according to the J-integral approach, along the front of a part through crack, initiated in correspondence of the outer surface of a hollow cylindrical specimen. The crack path is evaluated by using the Maximum Energy Release Rate (MERR) criterion, whereas the Paris' law is used to calculate crack growth rates. A numerical and experimental comparison of the results is presented, showing a good agreement in terms of crack growth rates and paths.

Keywords: Finite element method; Mixed-mode fracture; Crack propagation; Multiaxial fatigue.

*Corresponding author: Raffaele Sepe, e-mail: raffsepe@unina.it

Nomenclature

a	crack depth
b	crack advance measured at break through points
c	semi chord length
h	depth of the initial curvilinear edge notch
C, m	Paris equation constants
D	specimen external diameter
E	Young's modulus
G	shear modulus
J	J-integral
K_I, K_{II}, K_{III}	Mode I, II and mode III stress intensity factors
K_{eff}	effective stress intensity factor
ΔK_{eff}	effective stress intensity factor range
N	number of cycles
R	cyclic stress ratio
ν	Poisson's ratio
σ_{02}	monotonic tensile yield strength
δ	final elongation
ψ	final reduction of area
σ_u	nominal ultimate tensile strength
σ_t	true ultimate tensile strength
n	strain hardening exponent
α	strain hardening coefficient
db/dN	growth rate at break through points
da/dN	growth rate in the depth direction
a/D	relative crack depth
b/D	relative surface crack chord length

1. Introduction

Structural components, such as hollow shafts, can be subjected to multiaxial fatigue and the presence of notches can facilitate the onset of fatigue cracks. Consequently, for the shaft failure assessment it is mandatory the estimation of **critical crack length** and fatigue life. The prediction of the structural integrity of such cylindrical metallic components can be performed through fatigue growth numerical analysis, assuming initial and accumulated in service damages¹⁻².

Usually, part-through flaws start in correspondence of the free surfaces of cylinders and keeps, during the evolution, a quasi-elliptical³ shape. The cylindrical metallic components of engineering structures are frequently subject to combined loading conditions, including axial load, bending and torsion.

The Finite Element (FE) in combination with the Dual Boundary Element (DBE) methods represent a viable option to implement a global-local approach useful to investigate the fatigue behaviour of complex structural components undergoing complex loading conditions within acceptable computational time⁴⁻⁸.

Carpinteri et al.^{9,10} investigated a hollow metal cylinder affected by a circumferential elliptical surface-crack under different loading conditions, such as the bending-moment and the axial-loading, through numerical models based on 3D Finite Elements.

Predan et al.¹¹ estimated, by means of the FE method, the stress intensity factors (SIFs) for circumferential semi-elliptical surface cracks involving the cross section of a hollow cylinder under torsion.

Citarella et al.¹²⁻¹⁶ investigated the crack propagation in hollow shafts under torsion loading and combined axial-torsion loading conditions using both DBE and FE methods.

Shahani and Habibi¹⁷ carried out a study on the mixed-mode fracture induced by a semi-elliptical circumferential surface-crack lying on the external surface of a hollow cylinder cross-section; SIFs were numerically calculated through a FE model consisting of hexahedral 20 node-isoparametric elements and a singular form of these finite elements at the crack's front.

In this work, experimental tests and three-dimensional crack propagation simulation by FEM have been carried out on a hollow cylinder undergoing axial and combined axial-torsion loading conditions. Experimental tests have been carried out to obtain realistic data on the crack propagation: the samples have been tested under in-phase constant amplitude axial and torsional loading conditions.

SIFs along the front of an initial part through crack, started from the outer surface of the hollow cylinder, are calculated via the J-integral approach rather than Crack Tip Opening Displacement (CTOD), being the former more accurate and less dependent on mesh refinement level^{13,18}.

The crack path assessment is performed by using the maximum energy release rate criterion^{13,18} whilst the crack growth rates are calculated by the Paris' law, calibrated for the material under analysis.

The comparison between the predicted and experimental results showed a good agreement in terms of crack growth rates and paths.

2. Materials and experimental set-up

Dimensions and geometry of a hollow cylindrical specimen are shown in Fig. 1; in particular, the diameters D and d of gage sections are equal to 28 mm and 10 mm respectively. Two types of specimens are considered, one with a circular notch and the other with an elliptical notch. The surface edge notches were cut by Electrical Discharge Machining (EDM), with initial depth $h = 3.0$ mm for both circular and elliptical shape. The crack front can be approximated by an elliptical curve with characteristic sizes c and a , where c is the semi chord length and a is the crack depth.

The size b is defined as the length, measured along the free surface, of the arc between the advancing crack break through point and the (initial) notch break through point. Two type of fatigue tests were carried out:

- Axial load fatigue tests on specimens with circular and elliptical notch,
- Combined axial/torsion tests on specimens with elliptical notch.

The fatigue tests were carried out under load control, with a frequency of 10 Hz, at room temperature and with stress ratio $R = 0.1$, by means of a multiaxial testing machine (Fig. 2). The testing machine is equipped

with an axial torsional load cell having an axial and a torsional full scale of 100 kN and 2.0 kN·m respectively.

Axial load fatigue tests were carried out applying a maximum nominal load equal to $P = 35$ kN, whereas combined fatigue tests were performed applying in-phase and synchronous axial and torsion loads, with maximum values equal to $P = 40$ kN and $M_t = 250$ N·m respectively.

During test, the stress ratio was modified from $R = 0.1$ to $R = 0.5$ for a few cycles in order to create beach marks on the fracture surface that could be detected in a post mortem fractographic analysis; such stress ratio variation was iteratively applied each time the surface crack arc length increased of $\Delta b \cong 1$ mm (Fig. 3).

In order to measure the crack arc length b on the free surface an optical zoom microscope was used, whereas to measure the crack opening displacement a COD gauge was applied on the specimen cylindrical surface, in correspondence of the symmetry plane.

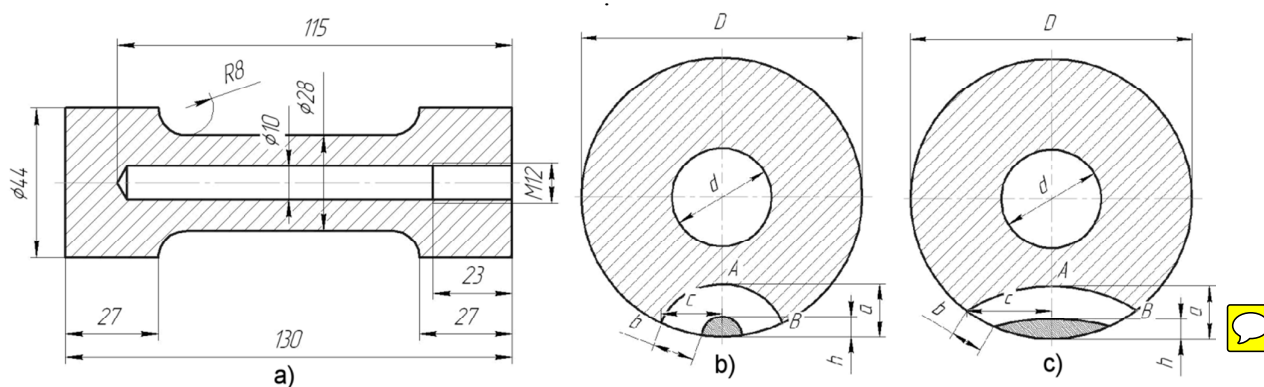


Fig. 1. Details of the hollow specimen: dimension and geometry a); initial circular notch b); initial elliptical notch c).



Fig. 2. Multiaxial testing machine.

The samples materials are aluminium alloys D16T (Al 2024) and B95AT (Al 7075). The mechanical properties are reported in Table 1, where: σ_{02} is the tensile yield strength, σ_u is the ultimate tensile strength, σ_t is the true tensile strength, ψ is the final percentage area reduction, δ is the percentage final elongation, E is the Young's modulus, n is the strain hardening exponent and α is the strain hardening coefficient.

Table 1. Mechanical properties of aluminium alloys at 20 °C.

Aluminum alloy	$\sigma_{0.2}$ [MPa]	σ_u [MPa]	σ_r [MPa]	ψ [%]	δ [%]	E [MPa]	n	α
D16T	438	594	665	11	11	76557	5.86	1.54
B95AT	520	586	775	36	14	75274	10.37	1.44

3. Experimental results

The typical fracture surfaces of different specimens are shown in Figs. 3 and 4 both for axial and axial-torsion loading, respectively.

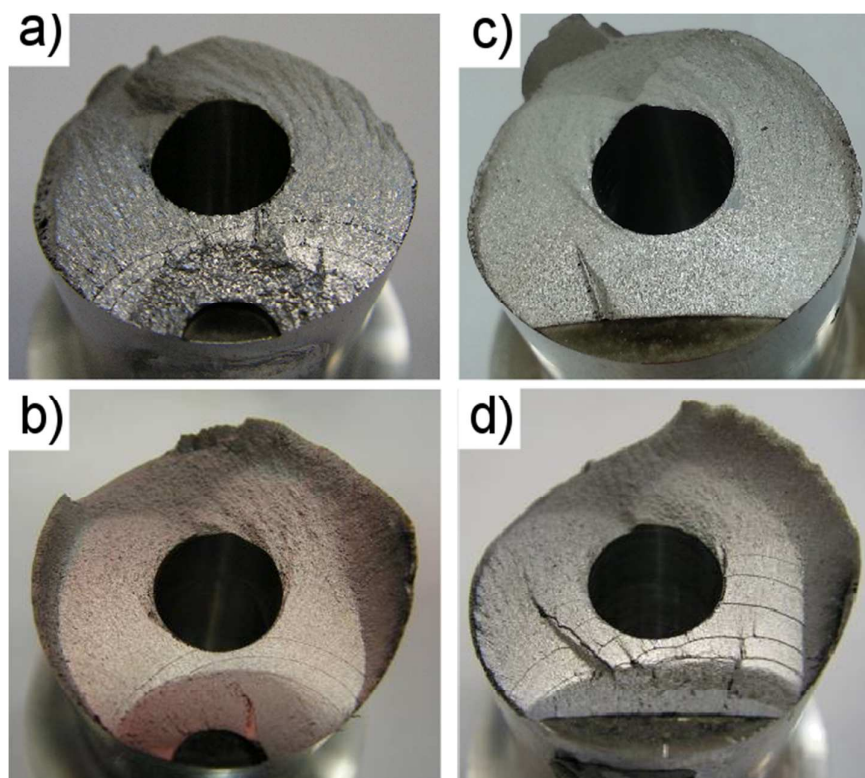


Fig. 3. Post mortem cross sections of specimens undergoing pure axial load: circular notch B95AT alloy a); circular notch D16T alloy b); semielliptical notch B95AT alloy c); semielliptical notch D16T alloy d).

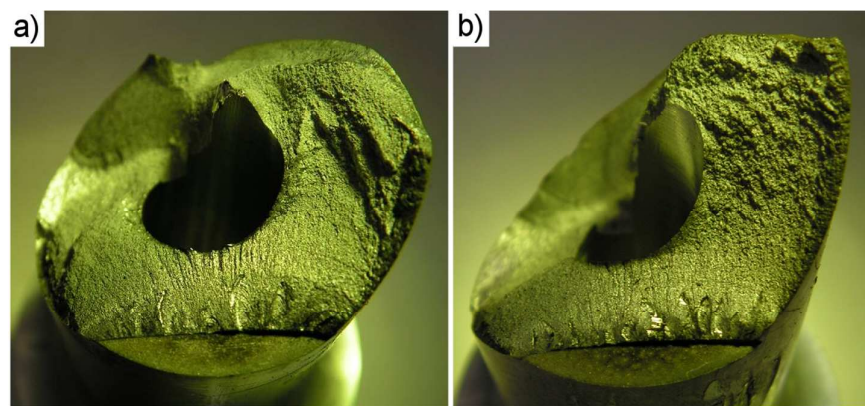


Fig. 4. Crack surface of specimens undergoing axial/torsion combined load: B95AT alloy a); D16T alloy b).

The crack growth rates were recorded using a zoom optical microscope and COD gauges. The crack front shape was obtained by metallographic post mortem analyses, as provided by the beach marks obtained by the previously mentioned periodic frequency change. In particular, using a comparison microscope, it was possible to obtain the relations between the dimensionless geometry parameters a/c and a/D (Fig. 5). In addition, the curve of surface crack propagation b versus cycle number N can be obtained (Fig. 6).

It was observed that in an initial phase of crack propagation its shape strongly depend on the initial geometrical flaw profiles, but, in a second phase, when the crack depth ratio a/D becomes larger than 0.25, the crack profiles converge to similar configuration (Fig. 5).

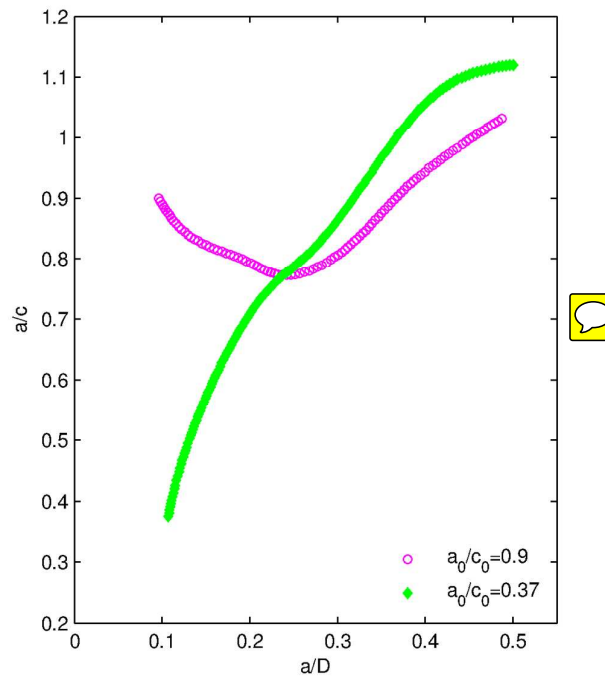


Fig. 5. Aspect ratio (a/c) vs. adimensional crack depth (a/d) for different initial surface flaw geometries considering the axial loading condition.

Fig. 6a shows plots of the curvilinear abscissa b against the number of cycles N , for axial fatigue tests on specimens with a circular or an elliptical notch. Fig. 6b shows the same parameter with reference to combined axial-torsion tests, carried out on specimens with an elliptical notch (in this case no samples with circular notch were considered).

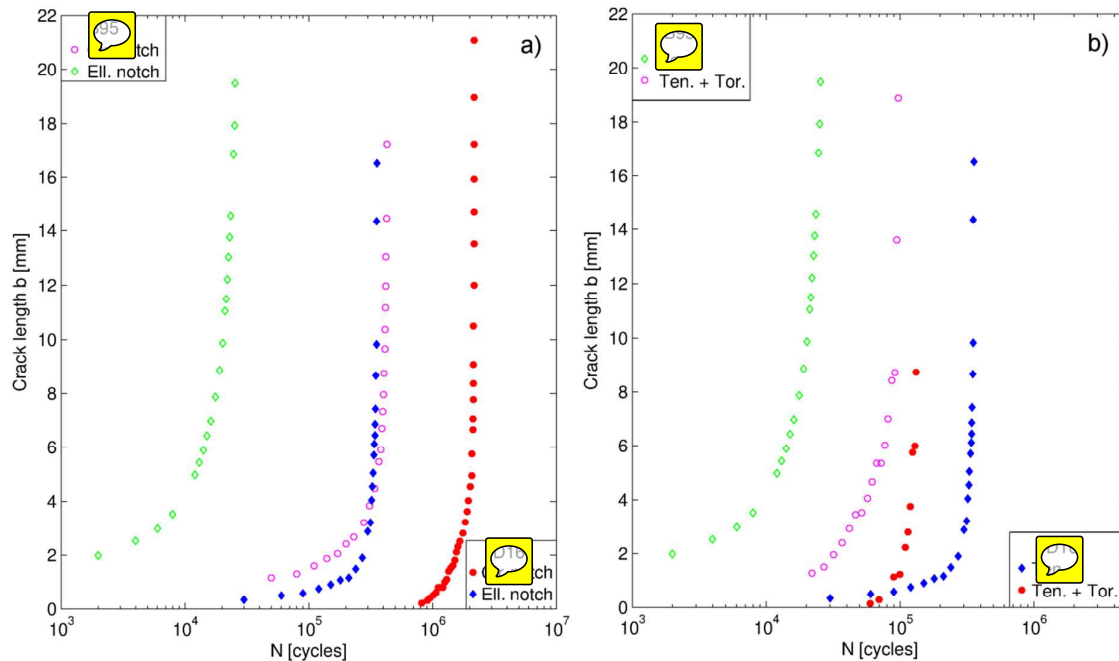


Fig. 6. Graphs of arc crack length b vs. cycles: under axial load with circular and elliptical notches a); under axial or combined axial/torsion loading with elliptical notch b).

As shown in Fig. 6a (axial load), the crack growth rates for the specimens (with circular and elliptical notch) made of B95AT are higher than those related to specimens made of D16T. As a matter of fact, considering an initial value of $b = 1.15$ mm for the circular notch, the number of cycles to failure are equal to 380203 and 810000 for B95AT and D16T alloy respectively, whereas, considering an initial value of $b = 2$ mm for the elliptical notch, the number of cycles to failure are equal to 23572 and 84902 for B95AT and D16T alloy respectively.

In case of elliptical notch, in-phase torsion loading superimposed to axial loading leads to an increase of crack growth rates for D16T and to a decrease for B95AT specimens (Fig. 6b). As a matter of fact, considering an initial value of $b = 2$ mm for B95AT and of 0.5 mm for D16T, the number of cycles to failure for B95AT are equal to 23288 and 65373 for axial and axial/torsion loading respectively, whereas the number of cycles to failure for D16T are equal to 84902 and 27500 for axial and axial/torsion loading respectively. These results are relevant because highlight that different materials exhibit opposite behaviour when torsional loading is superimposed to axial loading.

The relationship between the arc crack length b and COD with reference to the specimens undergoing pure axial load and combined axial/torsion loading are shown in Fig. 7. It is found that the arc crack length b can be correlated with COD for all the types of loadings and materials, using a unique fitting curve with a small scatter. This fact suggests the possibility of indirect crack length assessment from COD experimental measurements, at least in a first approximation.

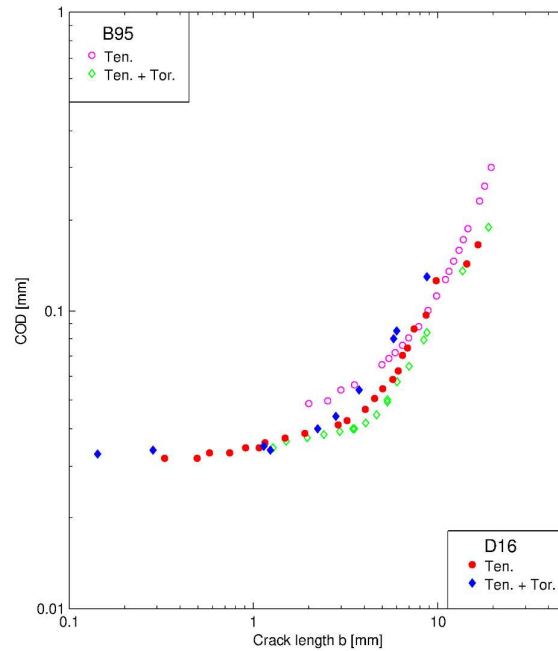


Fig. 7. *COD* vs. arc crack length b curve.

Fig. 8 shows the crack growth rate db/dN versus *COD*, or (indirectly) vs. b (due to the previously demonstrated correlation between b and *COD*), in case of pure cyclic axial and combined axial/torsion fatigue loading. In particular, it is found that for elliptical notches and different load cases and materials the experimental crack growth rates db/dN as a function of *COD* fits into four curves, whose relative position is consistent with the relative position of curves in Fig. 6b. It is interesting to observe the opposite impact of an added torsional load on crack growth rates along the external surface: for D16T and B95AT an acceleration rather than a small slowing down is respectively produced.

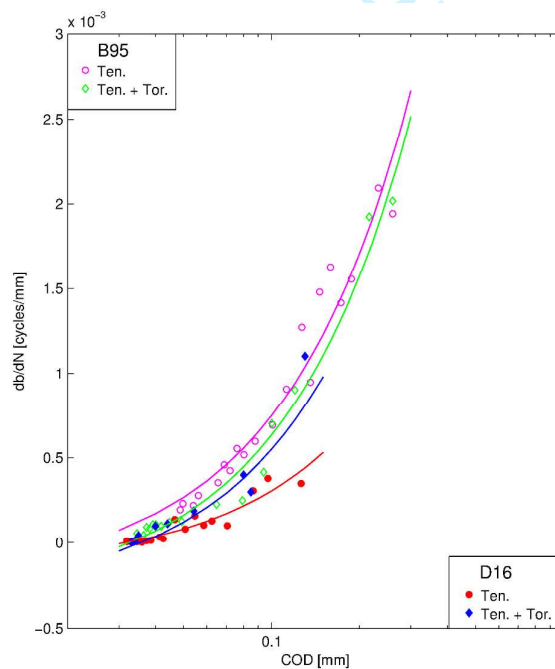


Fig. 8. Crack growth rate db/dN vs. *COD* under different loading conditions for specimen with elliptical notch.

4. Numerical analyses

A crack propagation simulation was just performed with reference to a D16T hollow cylindrical specimen with elliptical notch (Fig. 1c). The loading conditions of pure axial fatigue and combined axial/torsion fatigue were simulated.

A linear elastic fracture mechanics approach was used for these simulations. The numerical studies were based on finite element (FE) analyses using the adaptive remeshing approach. In this study, the commercial software ZENCRACK^{®19,20} has been adopted for automated 3D remeshing and crack propagation calculations along with ABAQUS^{®21} as finite element solver. The strategy used in this study is described in Citarella et al.¹⁴ and Maligno et al.²⁰.

The uncracked model (Fig. 9a) consists of 209020 elements and 226151 nodes, 209016 elements are hexahedral 8-nodes elements of type C3D8 and 4 are hexahedral 20-node elements of type C3D20 both with full integration (such elements define the volume portion that will be remeshed following the crack introduction). The updated FEM model, with crack introduction, is shown in Fig. 9b: the elements replacing the four aforementioned C3D20 elements are again hexahedral 20-node elements of type C3D20 with full integration (even if the mesh refinement is lower in the area surrounding the crack it is based on higher order interpolation elements).

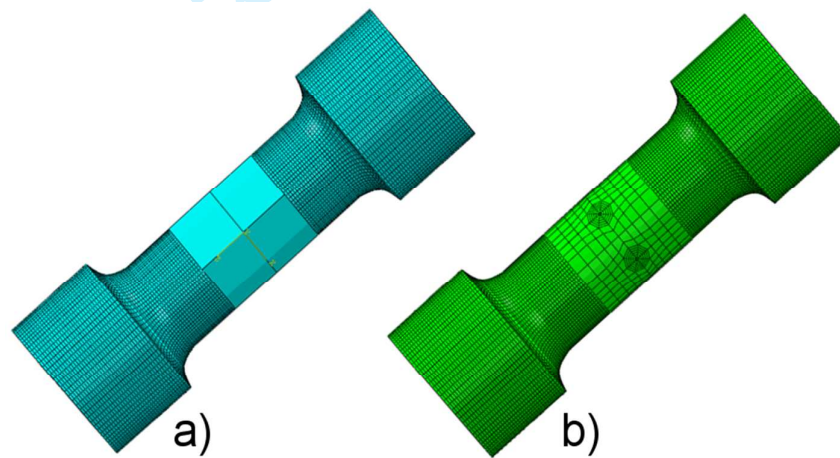


Fig. 9. Uncracked model a); cracked model b).

The Paris' law has been adopted to calculate the crack growth rate. The Paris' law is given by the following relationship:

$$\frac{da}{dN} = C \cdot \Delta K_{eff}^m, \quad (1)$$

where the material constants are: $C = 2.43416 \cdot 10^{-13} \text{ MPa} \cdot \text{m}^{0.5}$, $m = 3.325$. K_{eff} is an effective SIF, calculated from the mode I, mode II, and mode III K -values, as shown in the following. The crack propagation was simulated under constant amplitude load and stress ratio $R = 0.1$.

The strain energy release rate, obtained from the J-integral calculated by the FE solver, was used to drive crack growth calculations. The maximum energy release rate criterion was adopted to calculate the crack path.

There are several approaches to calculate SIFs such as: crack tip opening displacement (CTOD) approach^{22,23}, crack tip stress field approach²⁴ and SIF extraction method from J-integral^{13,18}. In the present work the SIFs are extracted from the J -integral based on the following equation:

$$J = \frac{B}{E} \cdot (K_I^2 + K_{II}^2) + \frac{1}{2G} \cdot K_{III}^2, \quad (2)$$

where $B = (1 - \nu^2)$ for plane strain and 1 for plane stress and G is the tangential modulus of elasticity.

The K_{eff} is calculated as in the following formula:

$$K_{eff} = \left(\frac{B}{E} \cdot (K_I^2 + K_{II}^2) + \frac{1+\nu}{B} \cdot K_{III}^2 \right)^{1/2}. \quad (3)$$

The crack propagation was simulated in two subsequent steps:

1. The first starting from the initial crack configuration up to the configuration in which the crack reaches the bore;
2. The second starting with two (wall-through) crack fronts and ending with the final failure.

5. Numerical results

• Axial Loading

The simulated crack propagation, from the initial crack up to the final scenario, is depicted in Fig. 10: the numerical simulation starts after the pre-cracking phase, with an initial crack corresponding to the first recorded crack front, after $N_0 = 30000$ cycles.

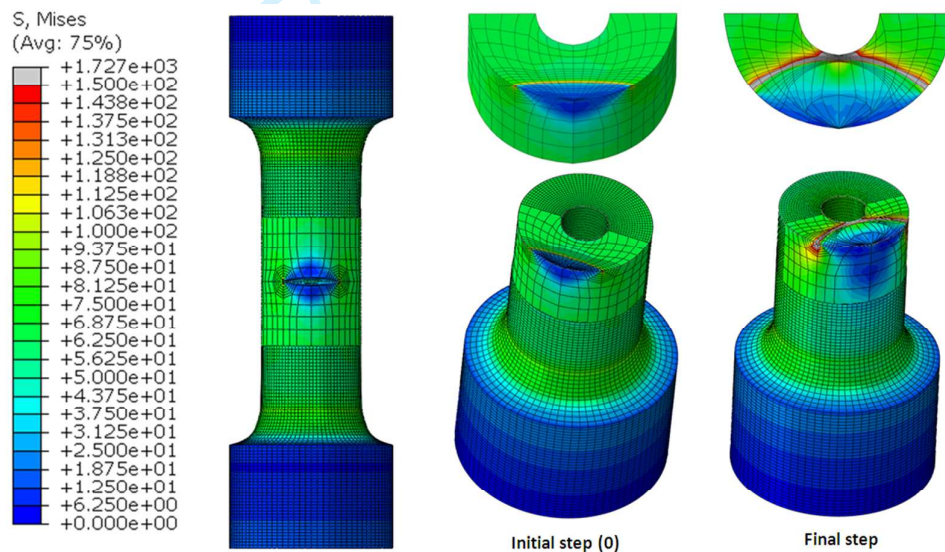


Fig. 10. von Mises stress scenario (MPa) for elliptical notch under pure axial load at different step of crack propagation.

• Combined Axial/Torsional Loading

Fig. 11 shows the crack propagation for the specimen under axial/torsion loading, starting from the initial configuration (step 0) up to the intermediate step when the crack reaches the bore. The numerical simulation starts after the pre-cracking phase, with an initial crack corresponding to the first recorded crack front, after $N_0 = 50000$ cycles. Fig. 12 shows crack propagation from the aforementioned intermediate step up to failure. In Fig. 12 the crack kinking induced by the modes II and III superposition, coming from the torsion load, is evident. A qualitative comparison between the numerical and experimental crack shape shows a satisfactory agreement (Fig. 12).

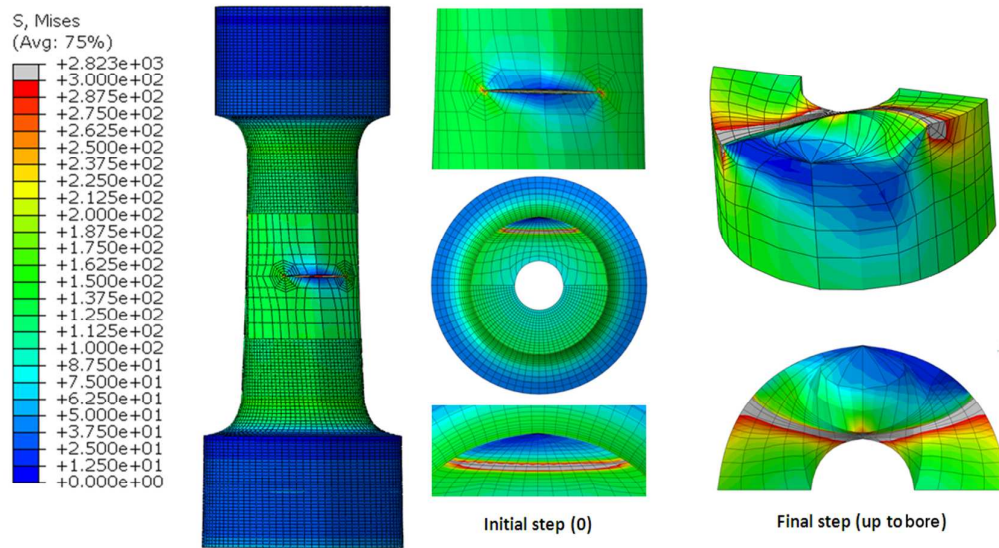


Fig. 11. von Mises stress scenario (MPa) for elliptical notch under axial/torsion loading at different step of crack propagation.

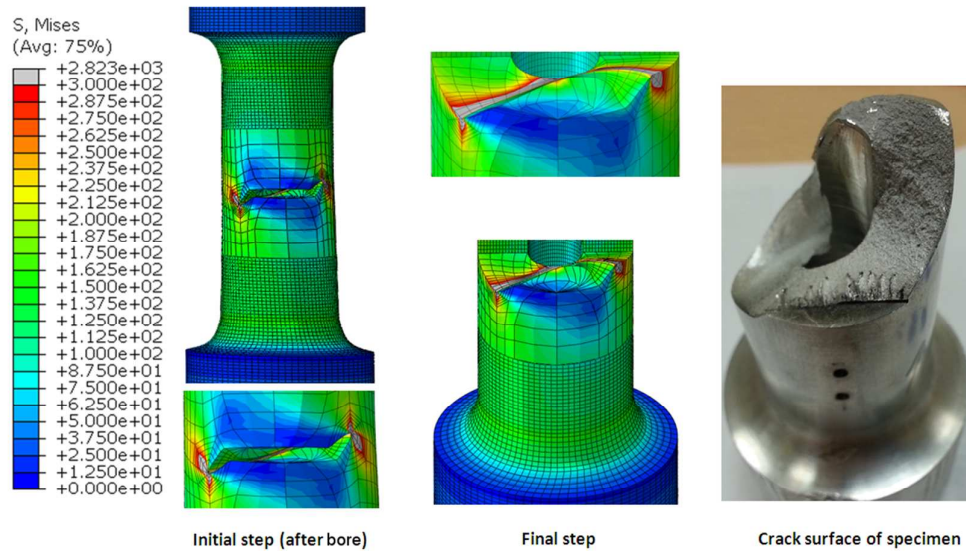


Fig. 12. von Mises stress scenario (MPa) for elliptical notch under axial/torsion loading at different step of crack propagation.

In Table 2 numerical and experimental results are shown, with reference to the number of cycles needed for the crack to reach the bore and from bore to final failure. A satisfactory agreement is displayed.

Table 2. Comparison of numerical and experimental results.

Notch shape	Loading condition	Number of cycles to reach the bore		Number of cycle to final failure	
		Exp.	Num.	Exp.	Num.
Elliptical	Axial	274210	287949	315000	310000
Elliptical	Axial/Torsion	---	77894	80000	80245

In Figs. 13-15 it is possible to appreciate the good level of correlation between experimental and numerical crack growth geometric parameters for both the analysed specimens.

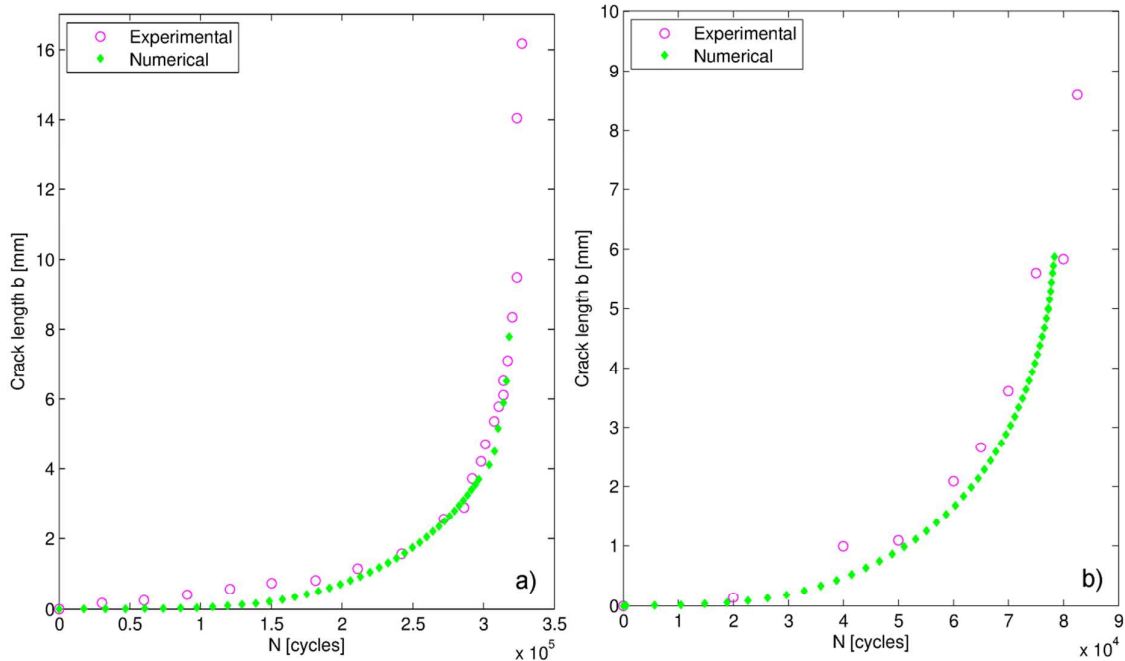


Fig. 13. Arc crack length b vs. cycles curve for specimens with elliptical notch: under axial load a) and axial/torsion loading b).

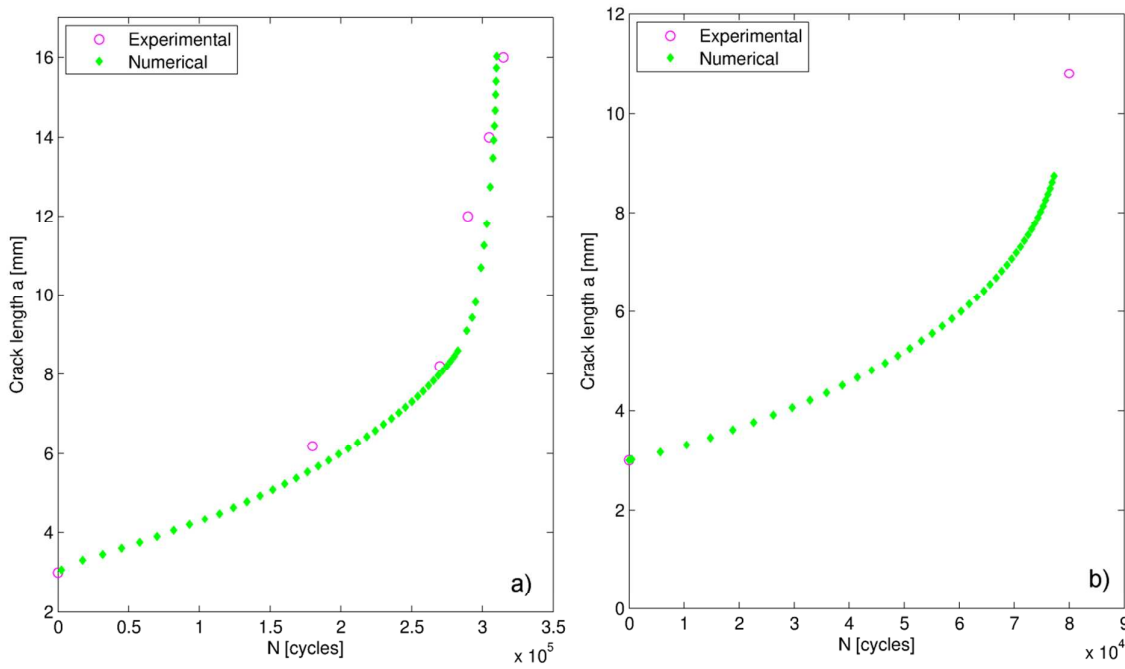


Fig. 14. Crack depth a vs. cycles curve for specimen with elliptical notch: under axial load a) and axial/torsion loading b).

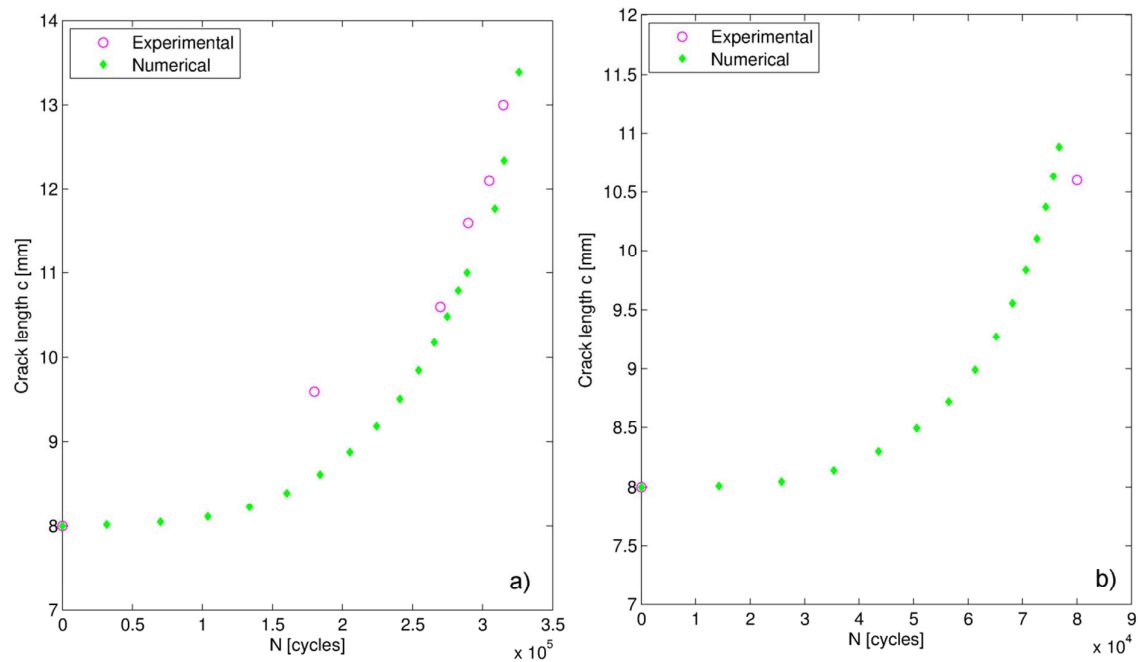


Fig. 15. Crack cord c vs. cycles curve for specimens with elliptical notch: under axial load a) and axial/torsion loading b).

K_I , K_{II} , and K_{III} values along crack front for the initial step (0), in case of pure axial load, are plotted in Fig. 16a: the crack propagates under pure mode I conditions because K_{II} and K_{III} values are negligible. Fig. 16b shows K_I , K_{II} , and K_{III} values along crack front at initial steps (0) for axial-torsion loading condition: due to the presence of torsion loading also Mode II and III crack conditions are generated along the initial crack front with relatively high K_{III} values.

6. Conclusions

In this study, fatigue surface crack growth rates for D16T (2024) and B95AT (7075) aluminium alloys were determined experimentally and numerically. The crack growth rates (considering the same loading conditions) for the specimens with circular and elliptical notch in B95AT are higher than those related to specimens D16T. In case of elliptical notch, superimposed in-phase torsion and axial loading conditions lead to an increase of crack growth rates for D16T and to a decrease for B95AT specimens. It has been also found that the crack length along the outer surface direction can be correlated with COD for all the types of loadings and materials using a unique fitting curve, with a small scatter: this fact suggests the possibility of crack length assessment from COD experimental measurements.

The computed FEM crack propagation results have been compared with the corresponding experimental ones; a good agreement has been achieved in terms of crack path and crack growth rates. Moreover, a complex 3D crack growth behaviour has been observed under superimposed axial/torsion loading. Specifically, it appears that the residual fatigue life decreases when an in-phase cyclic torsion is added to the cyclic axial load. This can be put in relation to the increase of the mode mixity. Furthermore, the FEM approach used by ZENCRACK[®] allows a reduction of the crack modelling preprocessing time thanks to the fact that it can be introduced easily and the propagation simulation is fully automatic (at each step the model is remeshed without the user intervention).

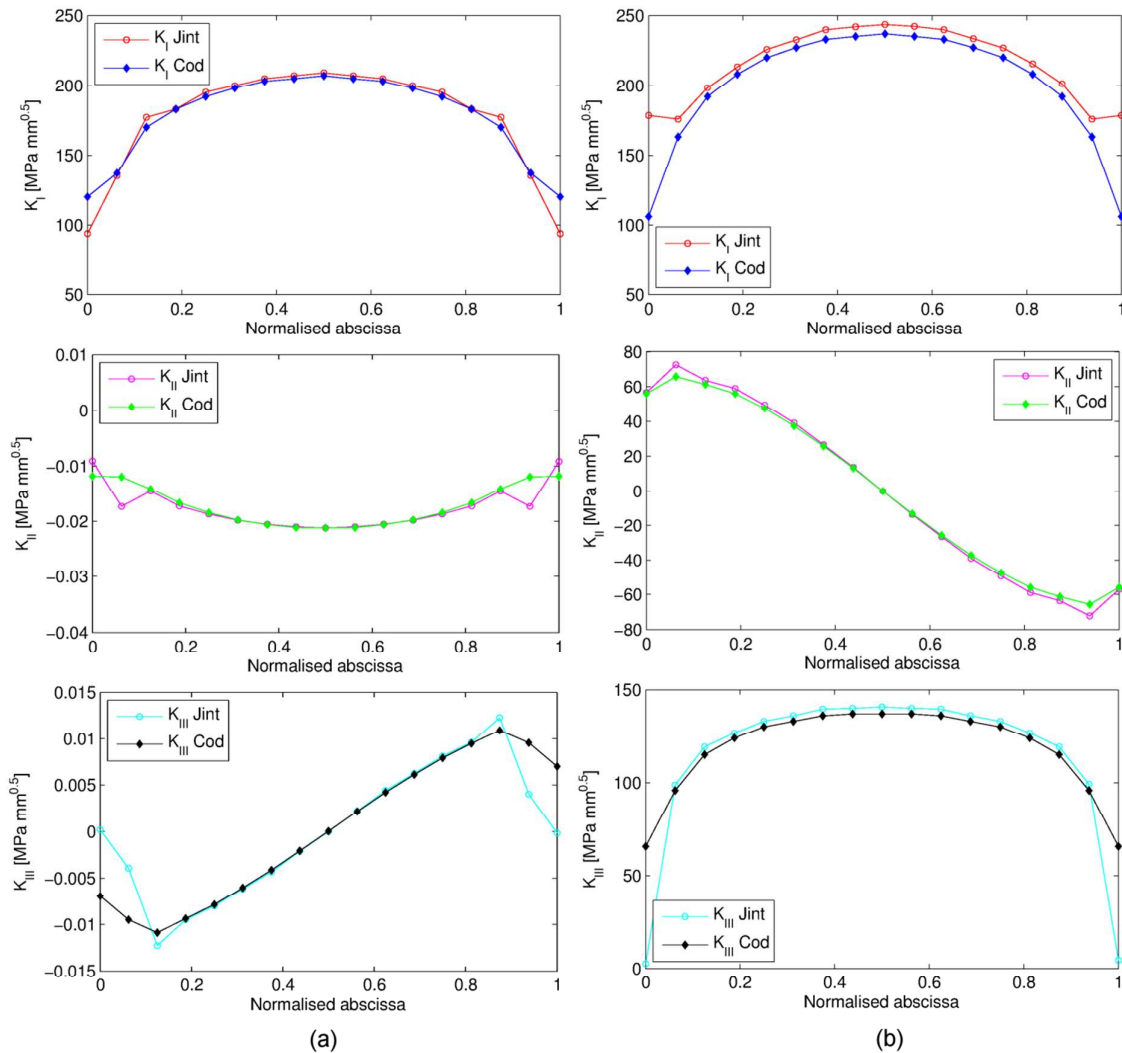



Fig. 16. SIFs [MPa·mm^{0.5}] along the crack front, as calculated by J-integral and COD approaches, for mode I (K_I), mode II (K_{II}) and mode III (K_{III}) at step (0): specimen under pure tension loading a); specimen under axial/torsion loading b).

Reference

1. Sahu, V. K., Ray, P. K., and Verma, B. B., Experimental fatigue crack growth analysis and modelling in part-through circumferentially pre-cracked pipes under pure bending load. *Fatig. Fract. Eng. Mater. Struct.* 2017; 40: 1154–1163.
2. YANG, F. and KUANG, Z., Fatigue crack growth for a surface crack in a round bar under multi-axial loading condition. *Fatig. Fract. Eng. Mater. Struct.*, 2005; 28: 963-970.
3. V.N. Shlyannikov, Fatigue shape analysis for internal surface flow in a pressurized hollow cylinder, *Int. J. Press. Vess. Pip.* 2000; 77: 227–234.
4. R. Citarella, G. Cricri, M. Lepore, M. Perrella, DBEM and FEM Analysis of an Extrusion Press Fatigue Failure. In: A. Öchsner, L.F.M. da Silva, H. Altenbach (eds.), *Materials with Complex Behaviour—Advanced Structured Materials*, 2010, Vol. 3, Part 2, 181-191. Springer-Verlag, Berlin, Germany, 2010.
5. V. Giannella, J. Fellingner, M. Perrella, R. Citarella, Fatigue life assessment in lateral support element of a magnet for nuclear fusion experiment “Wendelstein 7-X”, *Eng. Fract. Mech.* 2017; 178: 243–257.
6. Citarella, R., Giannella, V., Vivo, E., Mazzeo, M. FEM-DBEM approach for crack propagation in a low pressure aeroengine turbine vane segment. *Theor. Appl. Fract. Mech.* 2016; 86: 143-152.

7. R. Citarella, V. Giannella, M. A. Lepore, J. Fellingner. FEM-DBEM approach to analyse crack scenarios in a baffle cooling pipe undergoing heat flux from the plasma. *AIMS Materials Science*. 2017, 4 (2): 391-412.
8. Fellingner, J., Citarella, R., Giannella, V., Lepore, M., Sepe, R., Czerwinski, M., Herold, F., Stadler, R., Overview of fatigue life assessment of baffles in Wendelstein 7-X. *Fusion Eng. Des.* 2018; DOI: 10.1016/j.fusengdes.2018.02.011, Article in Press.
9. Carpinteri A, Brighenti R, Spagnoli A. Fatigue growth simulation of part-through flaws in thick walled pipes under rotary bending. *Int. J. Fatig.* 2000; 22:1–9.
10. Carpinteri A, Brighenti R. Circumferential surface flaws in pipes under cyclic axial loading. *Eng. Fract. Mech.* 1998; 60 (4): 383–96.
11. Predan, J., Mocilnic, V., Gubeljak, N., Stress intensity factors for circumferential semielliptical surface cracks in a hollow cylinder subjected to pure torsion, *Eng. Fract. Mech.* 2013; 105: 152–168.
12. V. Giannella, M. Perrella, R. Citarella, Efficient FEM-DBEM coupled approach for crack propagation simulations, *Theor. Appl. Fract. Mech.* 2017; 91: 76-85.
13. Citarella, R., Buchholz, F.-G., Comparison of crack growth simulation by DBEM and FEM for SEN-specimens undergoing torsion or bending loading, *Eng. Fract. Mech.* 2008; 75: 489–509.
14. Citarella, R., Lepore, M., Maligno, A., Shlyannikov, V., FEM simulation of a crack propagation in a round bar under combined tension and torsion fatigue loading. *Frattura ed Integrità Strutturale.* 2015; 31: 138-147.
15. Citarella, R., Lepore, M., Shlyannikov, V., Yarullin, R., Fatigue surface crack growth in cylindrical specimen under combined loading, *Eng. Fract. Mech.* 2014; 131: 439-453.
16. R. Citarella, V. Giannella, M. Lepore, G. Dhondt, Dual boundary element method and finite element method for mixed-mode crack propagation simulations in a cracked hollow shaft, *Fatig. Fract. Eng. Mater. Struct.* 2018; 41: 84–98.
17. Shahani AR, Habibi SE. Stress intensity factors in a hollow cylinder containing a circumferential semi-elliptical crack subjected to combine loading. *Int. J. Fatig.* 2007; 29: 128–40.
18. R. Citarella, G. Cricri, Comparison of DBEM and FEM Crack Path Predictions in a notched Shaft under Torsion. *Eng. Fract. Mech.* 2010; 77: 1730-1749.
19. Zencrack 7.9  2015. Zentech International Limited, UK.
20. Maligno, A.R., Rajaratnam, S., Leen, S.B., Williams, E.J., A three-dimensional (3D) numerical study of fatigue crack growth using remeshing techniques, *Eng. Fract. Mech.* 2010; 77: 94–111.
21. Dassault Systems Simulia Corp 2011. Abaqus analysis user's manual, Version 6.12.1. Providence, RI, USA.
22. Cali, C., Citarella, R., Perrella, M., Three-dimensional crack growth: numerical evaluations and experimental tests, *European Structural Integrity Society* 2003; 31: 3-504, *Biaxial/Multiaxial Fatigue and Fracture*, Edited by Andrea Carpinteri, Manuel de Freitas and Andrea Spagnoli.
23. Citarella, R., Perrella, M., Multiple surface crack propagation: numerical simulations and experimental tests, *Fatig. Fract. Eng. Mater. Struct.* 2005; 28: 135-148.
24. Dhondt, G., Application of the Finite Element Method to mixed-mode cyclic crack propagation calculations in specimens, *Int. J. Fatig.* 2014; 58: 2–11.